


Active learning accelerates electrolyte solvent screening for anode-free lithium metal batteries

Received: 11 December 2024

Accepted: 15 August 2025

Published online: 25 September 2025

 Check for updatesPeiyuan Ma^{1,2}, Ritesh Kumar^{1,2}, Ke-Hsin Wang¹ & Chibueze V. Amanchukwu¹✉

Anode-free or ‘zero-excess’ lithium metal batteries offer high energy density compared to current lithium-ion batteries but require electrolyte innovation to extend cycle life. Due to the lack of universal design principles, electrolyte development for anode-free lithium metal batteries is slow and incremental and mainly driven by trial-and-error. Here, we demonstrate the use of active learning as an alternative approach to accelerate electrolyte discovery for anode-free lithium metal batteries. Unlike conventional data-intensive frequentist machine learning techniques, our active learning framework employs sequential Bayesian experimental design with Bayesian model averaging to efficiently identify optimal candidates in typical data-scarce and noisy label settings. Using capacity retention in real Cu||LiFePO₄ cells as the target property, our approach integrates experimental feedback to iteratively refine predictions. Starting with just 58 data points from an in-house cycling dataset, the active learning framework explored a virtual search space of 1 million electrolytes, rapidly converging on optimal candidates. After seven active learning campaigns with about ten electrolytes tested in each, four distinct electrolyte solvents are identified that rival state-of-the-art electrolytes in performance. This work showcases the promise of active learning approaches in navigating large electrolyte chemical spaces for next-generation batteries.

Next-generation batteries are required to meet the energy-density requirements of applications such as electric vehicles, long-haul trucking, and electric aviation¹. Among next-generation electrode materials, the lithium metal negative electrode has attracted great research interest because of its high specific capacity (3860 mAh/g) and low electrochemical potential (−3.04 V versus standard hydrogen electrode)². While lithium metal batteries (LMBs) based on a lithium metal negative electrode and layered oxide positive electrode can theoretically achieve ~50% higher energy density than current lithium-ion batteries (LIBs), the high chemical reactivity and low deposition/stripping reversibility of lithium metal have limited their cycle life². As a result, excess lithium metal is commonly added

to extend cycle life in existing literature on LMBs, which decreases energy density and causes added safety concerns, especially during transport³. Recently, so-called “anode-free” or ‘zero-excess’ batteries – configured with only a bare current collector on the negative electrode side – have emerged as an attractive alternative for LMBs as the energy density can be maximized^{3,4}. The industrial fabrication of anode-free LMBs is also simpler because it can take advantage of current LIB infrastructure, and can be safer for transport because the cell does not initially contain the lithium metal. Unfortunately, extending cycle life of anode-free LMBs is even more challenging since there is no reservoir of lithium metal to compensate for capacity loss^{4–6}.

¹Pritzker School of Molecular Engineering, University of Chicago, Chicago, IL 60637, USA. ²These authors contributed equally: Peiyuan Ma, Ritesh Kumar.

✉ e-mail: chibueze@uchicago.edu

Among the many different approaches to improve the cycle life of anode-free LMBs, electrolyte development stands out as the most promising pathway because the solid electrolyte interphase (SEI) generated from electrolyte degradation is widely believed to play a key role in modulating lithium metal cycling stability^{7–9}. For example, localized high concentration electrolytes (LHCEs) that utilize a high salt to solvent molar ratio and non-solvating fluoroether diluents are reported to achieve improved anode-free LMB cycle life due to the formation of anion-derived SEI¹⁰. In addition, electrolytes composed of fluoroethylene carbonate (FEC), diethyl carbonate (DEC), lithium difluoro(oxalato) borate (LiDFOB), and LiBF₄ have also been reported to enable long cycle life in anode-free LMBs^{3,11}. Recently, fluorinated ether solvent-based electrolytes have been developed and optimized for anode-free LMBs, where the high lithium metal Coulombic efficiency and long cycle life are attributed to a lithium solvation sheath rich in anions^{12,13}. However, the reported electrolyte systems are very distinct in composition and design strategies. Hence, electrolyte discovery is primarily guided by trial-and-error, and it is difficult to chart a path forward.

Recently, artificial intelligence (AI)-based approaches have become promising tools for materials discovery¹⁴. While data science is widely used in drug discovery^{15,16}, its adoption in battery research, especially for liquid electrolytes, is still emerging^{17,18}. Frequentist AI techniques often require large datasets, posing a challenge for emerging technologies like anode-free LMBs, where data is scarce and experimental measurements are often noisy. Human experts use intuition to generate hypotheses, but current machine learning (ML) algorithms lack this and can make overconfident predictions with sparse data¹⁸. Alternatively, Bayesian approaches are well-suited for handling noisy data, as they explicitly quantify prediction uncertainty. This allows them to better guide experiments by identifying hypotheses with higher success potential and alerting researchers to unexplored, riskier experiments, even in the presence of experimental variability. This was demonstrated by Attia et al.¹⁹, who performed efficient optimization of experimental design with fast-charging protocols for LIBs, significantly reducing the time and number of experiments required. Compared to physical parameter optimization^{19,20}, electrolyte discovery offers an opportunity for substantial improvement in battery performance but is more challenging due to the enormous and diverse chemical space of unexplored organic compounds, as well as its discrete and high-dimensional nature. Previous efforts in battery materials discovery have primarily focused on optimizing computational target properties without experimental validation^{21–23}, or on experimentally optimizing properties for LIBs^{24,25} and redox flow batteries²⁶.

In this work, we utilize a sequential Bayesian experimental design, also referred to as active learning (AL) approach, to enable efficient electrolyte discovery for anode-free LMBs. As a starting point, an in-house dataset of 58 anode-free LMB cycling profiles was used as an initial dataset to train Gaussian process regression (GPR) surrogate models with four different covariance kernels (prior functions). The Bayesian model averaging (BMA)^{27,28} approach was used to help alleviate inaccuracy and overfitting typically associated with such small datasets. A search space of 1 million electrolytes was constructed with individual electrolyte solvent candidates filtered out from PubChem and eMolecules databases and paired with 1 M lithium salt. The AL workflow was leveraged to find optimal electrolytes for Cu||LFP (Cu||LiFePO₄) anode-free LMB from the virtual search space using cell capacity retention as the target property for optimization. Unlabeled electrolytes suggested by the AL framework were experimentally tested, and the resulting battery cycling data were iteratively fed back to the model. After 6 campaigns with about 10 commercially purchased compounds labeled in each campaign, ether electrolytes were consistently identified as the most promising for anode-free LMBs from the chemical space by the oracle component of AL. We then sampled 6 compounds using greedy selection and subsequently synthesized and tested them. From the overall AL workflow, we investigated four different electrolyte solvents

in detail that show performance that rivals state-of-the-art anode-free electrolytes. Analysis of the electrolyte solvation structures and SEI composition revealed similarities to the previously reported high-performing electrolytes. Therefore, the workflow allows for accelerated discovery of compatible electrolytes for anode-free batteries within a manageable expenditure of time and resources, while also generating indispensable datasets for training other frequentist ML models in the future. Finally, our work illustrates the feasibility of the AL approach in screening electrolyte candidates for improved battery cycling performance, even in data-scarce and noisy label regimes.

Results

Design of experiments (DoE) for electrolyte optimization; datasets, and virtual search space

Anode-free LMB refers to a battery configuration where only a bare current collector is present on the negative electrode side when the cell is assembled (Fig. 1a). During charging, lithium metal is deposited on the current collector and serves as the negative electrode. Upon discharge, lithium metal is stripped (electro-dissolution). Anode-free LMBs reported in the literature are usually based on either layered oxide positive electrodes (LiMO₂) or lithium iron phosphate (LFP, LiFePO₄) positive electrode with a Cu-based current collector (Table S1). While layered oxide positive electrodes such as NMC811 (LiNi_{0.8}Mn_{0.1}Co_{0.1}O₂) are preferred in reported studies due to their higher energy density than LFP positive electrode, the high operation voltage and structural instability often leads to parasitic reactions at the positive electrode, which induces complex cross talk effects^{29,30}. To reduce complexity and focus primarily on improving lithium metal cycling stability, Cu||LFP was selected as the standard testing configuration. While the goal for promoting battery cycle life is clearly to maintain higher capacity at longer cycle number, it can be difficult to select a single parameter to quantify cycling performance. Lithium Coulombic efficiency measured in Li||Cu cells is the most frequently used descriptor for lithium metal cycling performance with recent ML models built for its prediction^{31–33}. However, as literature⁶ and our data (Fig. S1) show that Li||Cu Coulombic efficiency do not necessarily correlate with capacity retention in actual anode-free LMBs. Hence, we focus on the prediction of capacity retention. Figure 1b shows several typical capacity retention curves of Cu||LFP cells using different electrolytes, where significant capacity loss can occur in the initial cycle and/or accumulate gradually in the later cycles. For example, curve i and curve v in Fig. 1b have similar capacity decay slope in the later cycling but have very different capacity in the first two cycles; Curves ii, iii, and iv have similar initial capacity but diverged in the later cycles. To account for both initial capacity and long-term cycling stability effects and limit time cost as well as to allow the data-driven framework to distinguish inherent differences between positive electrode types, discharge capacity at 20th cycle normalized with respect to positive electrode theoretical capacity (C_{norm}^{20}) was selected as proxy for overall performance and target property for optimization. Our aim is to discover optimal electrolytes solely based on their identity, without relying on additional experimental or computational characterizations.

To perform optimal experimental design of electrolytes for anode-free LMBs, first, the virtual search space must be defined on which the optimization is to be carried on. As shown in Fig. 1c a large chemical search space consisting of unlabeled small organic molecules from eMolecules and PubChem databases were used for this purpose. Further filtration based on removing undesirable chemical moieties, non-synthesizability, and low conductivity were performed, as discussed in Supplementary Note 1 to refine the search space. Our design of experiments (DoE) workflow, with the aim of optimizing (maximizing) discharge capacity of anode-free LMBs by identifying promising electrolytes using AL, is illustrated in Fig. 1d and discussed in detail in Supplementary Note 2. To carry out the sequential optimization, initial labeled training data is needed³⁴. Due to the limited number of anode-free LMB cycling data and very different testing

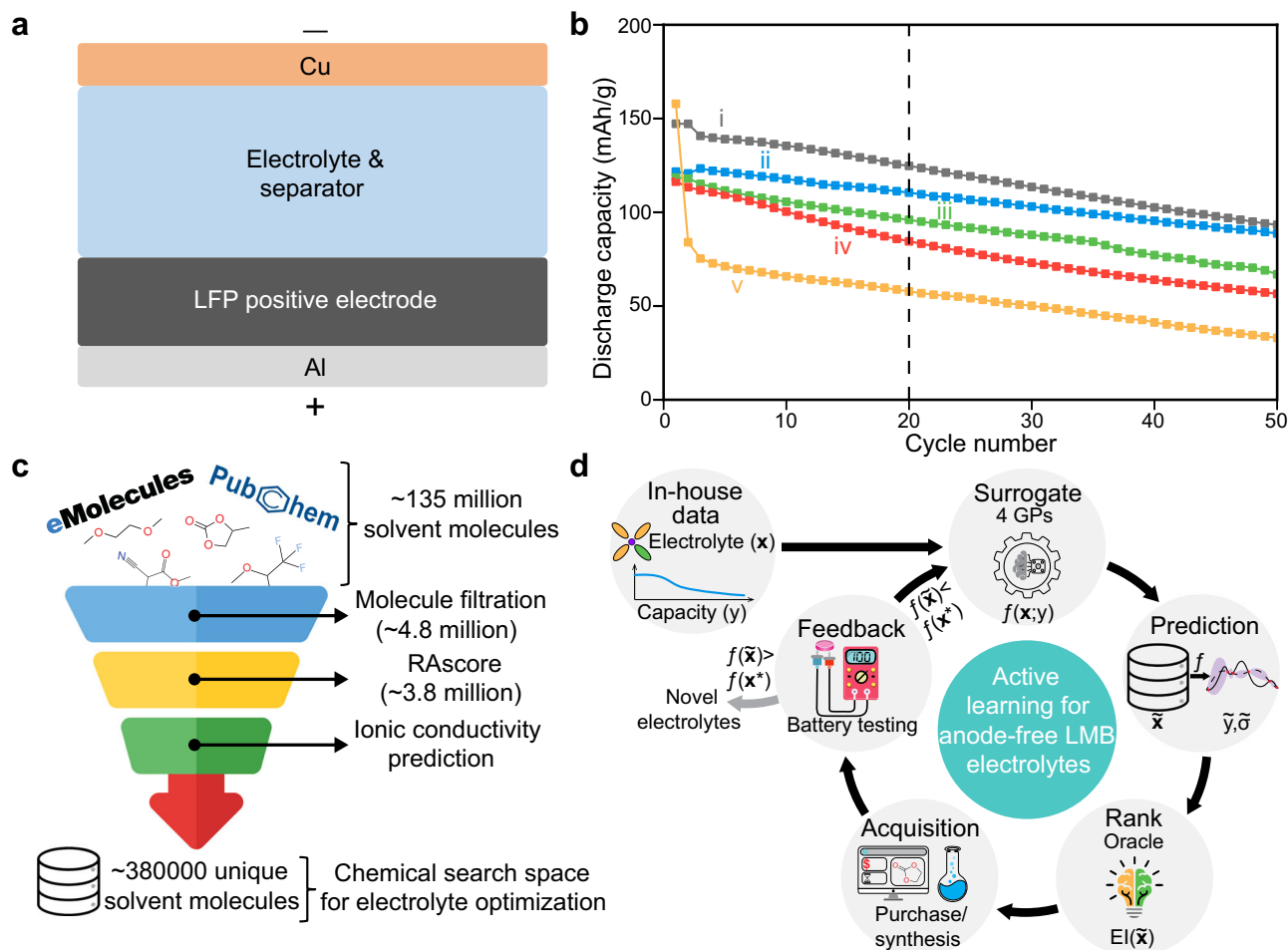


Fig. 1 | Background and design of experiments (DoE) formulation. **a** Schematic illustration of Cu || LFP cell configuration as an example of anode-free lithium metal batteries (LMBs) utilized in the present study. **b** Illustrative examples for anode-free LMB capacity retention curves. The curves shown do not represent real data. Discharge capacity at 20th cycle normalized with respect to positive electrode theoretical capacity is selected as target property to balance the effects of initial Coulombic efficiency and long-term stability. **c** Workflow describing creation of the virtual search space. **d** Schematic illustration of the active learning workflow, consisting of five steps in an iterative closed-loop, leading to batched optimization

of liquid electrolytes compatible with anode-free LMBs – training of surrogate models, inference on virtual search space (unlabeled), ranking of predicted candidates by the oracle (acquisition function), acquiring purchasable/synthesizable candidates, experimental battery testing, and feedback to the surrogate models. GPs = Gaussian processes, (\mathbf{x}, y) = input features and labels (normalized discharge capacity at 20th cycle) for in-house dataset; $(\tilde{\mathbf{x}}, \tilde{\mu}, \tilde{\sigma})$ = input features, predicted mean and uncertainty for electrolyte target property in virtual search space, \mathbf{x}^* = best observed value, and EI = expected improvement.

conditions used in literature (Table S1), we collected an in-house dataset containing 58 individual anode-free LMB cycling profiles in coin cell configuration and consistent cycling protocols. As shown in Table S2 and Fig. S1, the majority of this in-house dataset are single-solvent-single-salt electrolytes based on ether solvent (22 out of 26 unique solvent molecules) and 1 or 2 M Lithium bis(fluorosulfonyl) amide (LiFSA) salt, which also reflects the literature trend that LiFSA/ether combination enables the best anode-free LMB performance in single-solvent-single-salt electrolytes^{12,13,35–37}. The quality of in-house dataset is analyzed by standard deviation among replicated tests. For example, three replicated tests of 1,2-dimethoxyethane with 2 M LiFSA in Cu || LFP cell show a standard deviation of 5.6% and four replicates of 1,1,1,2,2-pentafluoro-3-(2-methoxyethoxy)propane with 1 M LiFSA in Cu || LFP cell show a standard deviation of 8.2%, which are comparable to literature^{3,13}. However, unlike later data (optimization batch 1 to 7) that were collected in standard conditions, we should note that the in-house dataset do contain varied conditions, such as salt concentration of 2 M, NMC positive electrode, and higher temperature. To account for such heterogeneity, the in-house dataset was featurized (details in Supplementary Note 3) before being used as initial training data for the AL workflow. Any optimization using the AL framework involves

choosing two crucial components – the surrogate model and the acquisition function. Given the small dataset size and the lack of prior knowledge about the underlying relationships, relying on a single surrogate model may lead to suboptimal exploration or exploitation. To address this, we employed a Bayesian Model Averaging (BMA) approach, which integrates predictions and uncertainties from multiple surrogate models to balance the strengths and weaknesses of individual models^{27,38}. Specifically, we selected four Gaussian processes (GPs; explained in Supplementary Notes 4 and 5) with different covariance kernels to capture diverse relationships in the chemical space and input data. The surrogate models, once trained on labeled data, yield predictions and uncertainties on the unlabeled data points, which are fed to the acquisition function (expected improvement (EI) chosen in this work; described in Supplementary Note 6). The electrolyte solvent molecules suggested by the acquisition function were tested for battery performance upon purchasing or synthesizing. The tested molecules were removed from the virtual search space in subsequent batches to prevent reselection of such molecules. To save resources and time and to focus on new solvent discovery, battery testing is performed only for solvent compounds paired with LiFSA because it can dissolve in a wide range of solvents, supports high ionic

conductivity, and supports high Coulombic efficiency (CE) in LMBs^{12,13,35–37}.

Progress of sequential optimization using the AL framework

The AL workflow identifies promising candidates for battery testing by exploring the search space and optimizing selection. This process focuses on the probability of improving upon the current best estimate of the target property by sampling from the available compounds. When there is minimal uncertainty in predicted estimates, the algorithm prioritizes samples with properties better than the best measured value so far (exploitation). In contrast, with high uncertainty, the algorithm focuses on selecting samples with the greatest uncertainty (exploration), rather than solely seeking those with optimal properties. For intermediate values, the algorithm balances exploration and exploitation to avoid getting trapped in local maxima. As a result, it shifts toward regions with greater uncertainty after the most promising local samples have been tested. The effectiveness of this approach depends on the performance of the surrogate GP models, which evolve over successive batches of optimization. As shown in Fig. S2a, the performance of the individual surrogate models fluctuates across batches, while the average performance exhibits a slight decline from the initial batch to batch 5. However, the surrogate models are overfitted initially, evident by their out-of-batch performance shown in Fig. S2b, where average errors are high in batch 1 and then decrease subsequently. There is also a large variance among the performance of four GPs with different prior kernels in the initial batches (Fig. S2a), but all models approach the same performance at batch 6 (even for out-of-batch performance, Fig. S2b). The difference in average performance of models between in-batch (root mean squared error; RMSE = 0.20) and out-of-batch (RMSE = 0.26) data are small in the case of batch 6, signifying that surrogate models in batch 6 have attained optimal performance. The suggestions from the AL framework span across a wide variety of functional group classes (discussion on assigning functional groups described in Supplementary Note 1), as shown through t-distributed stochastic neighbor embeddings (t-SNE) plots in Fig. 2a for selected batches (refer to Fig. S3 for all batches and to Fig. S4 for bar plots showing distribution of functional group classes). Initially, the AL framework picks several candidates belonging to amides, amines, and imides, even though such molecules were not present in the in-house dataset, due to the higher uncertainty associated with them. The oracle preferred these uncertain regions to find diverse compounds in pursuit of finding global minima (exploration).

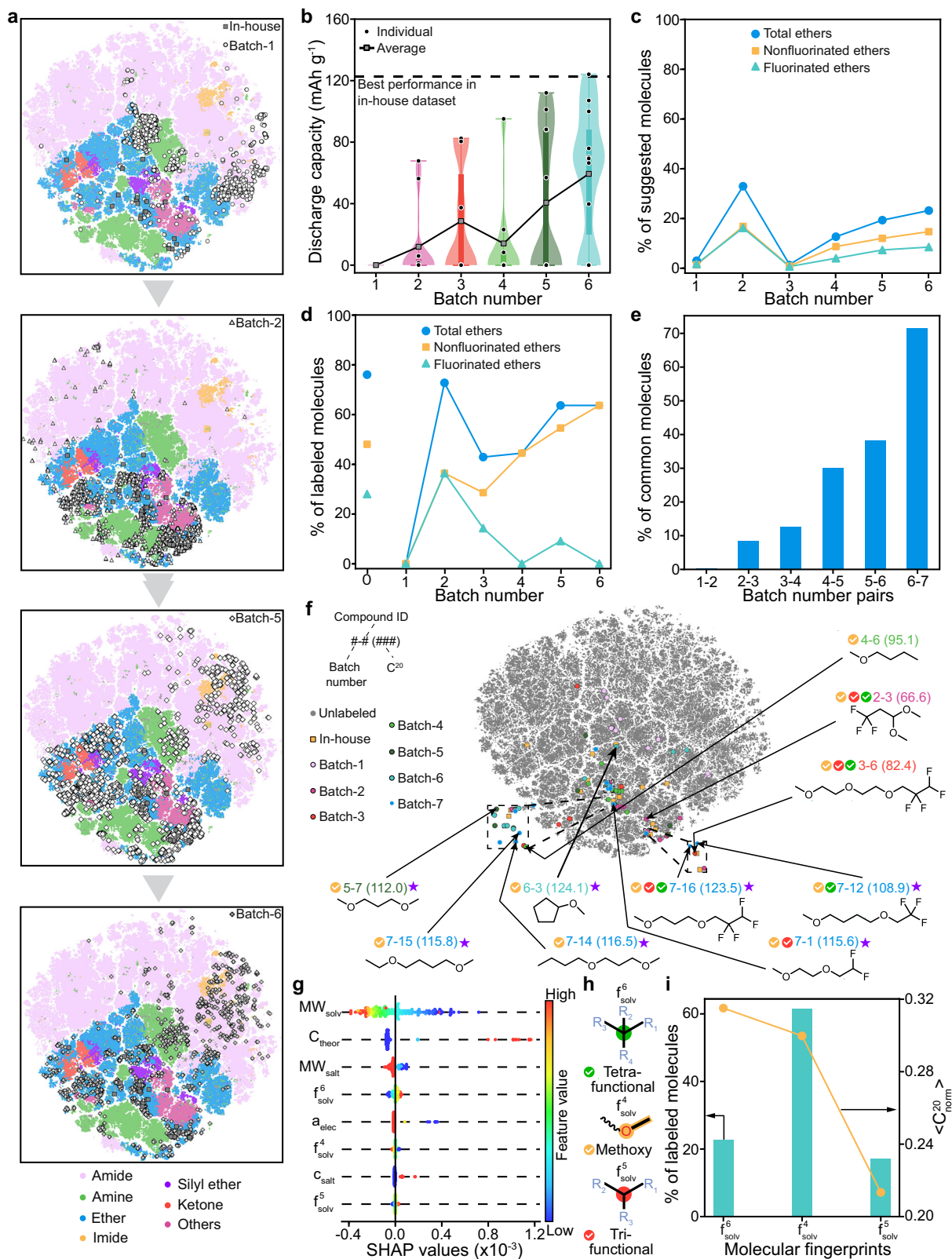
Due to the use of four surrogate models, aggregated EI (EI^{aggr} ; equation S9) obtained using the BMA technique (Supplementary Note 7) was used to rank suggested molecules. To evaluate how the AL framework transitions from exploration to exploitation behavior, the distribution of aggregated uncertainty (σ^{aggr}) values (defined in equation S11) for suggested compounds in each batch is shown using violin plots in Fig. S5a. As expected of performing AL using the EI acquisition function, the initial batches prioritize exploration, while later stages favor exploitation. The median of σ^{aggr} values (depicted by circles in each violin) decreases steadily across successive batches and eventually plateaus between batches 5 and 6. During the first batch, the aggregated uncertainties are higher, thereby resulting in high EI^{aggr} (violin plot in Fig. S5b for all batches) and a higher tendency for exploration. The decrease in σ^{aggr} in subsequent batches contributes to a reduction in EI^{aggr} and preference for exploitation over exploration. The trend can be further corroborated through the t-SNE plots depicting exploitation ratio ($r_{exploit}$) defined in equation S13 in the SI, as shown in Fig. S6. These plots show that, in subsequent batches, points with higher exploitation ratios tend to cluster closer to the training data. This indicates that the AL framework is successfully focusing on regions where higher target properties are found, highlighting the promising areas for anode-free battery electrolytes.

Progress of acquisition using AL suggestions

From the list of solvent molecules suggested by the AL framework obtained through trade-offs in exploitation and exploration strategies, about 10 compounds are selected and tested based on following criteria: (1) commercially purchasable (available in the United States with price < \$1000/g and lead time < 2 weeks; further details in Supplementary Note 2) solvent molecules are prioritized in the first 6 batches to accelerate progress; (2) when multiple similar compounds are recommended (such as methyl propyl ether, methyl butyl ether, methyl pentyl ether and methyl hexyl ether), only half of them with higher ranking are tested to promote diversity in the labeled dataset; (3) screening is performed sequentially, starting with the highest-ranked molecules and continuing until the desired number of purchasable candidates is selected, typically from the top 5,000 but not exceeding the top 10,000 ranked molecules; (4) chlorine containing compounds are purposefully omitted after batch 5 because all chlorinated solvents tested in previous batches show poor electrochemical profiles indicating continuous electrolyte degradation (Fig. S7). For each batch, selected compounds are purchased, paired with 1 M LiFSA in Cu || LFP cells and their discharge capacity data at 20th cycle is measured and fed to the surrogate model in the next AL campaign.

All the solvent molecules selected based on the AL suggestions are listed in Table S3 and shown in Fig. S8 and S9, with most of them procured from commercial vendors. For batch 3, only 5 commercially available molecules were found in the top 10,000 rankings. Therefore, we selected two highly ranked compounds (3-6, 7th and 3-7, 214th) that are synthesizable in one step to supplement the labeled dataset. As Fig. S10 shows, not all selected molecules can fully dissolve 1 M LiFSA salt, and the performance of such electrolytes was arbitrarily assigned as 0. Incorporating models that enable salt solubility predictions to filter out such compounds would be of significant interest for a follow-up work³⁹. For some electrolytes that cannot finish the first cycle in Cu || LFP cell (Fig. S7), their performance was also marked as 0. Figure 2b summarizes the performance of individual electrolytes acquired in each batch, their distribution, and the average performance of all electrolytes in each batch. Despite the presence of a few poor-performing electrolytes in all batches, the average performance, the distribution of higher discharge capacities, and the best performance from each batch improved steadily. From batch 6, the best performing electrolyte (6-3) enables an average discharge capacity of 124 mAh/g at the 20th cycle, which reaches the best performance in the in-house dataset.

Interestingly, the best performing electrolytes from batch 2 to 6 are all based on ether compounds with molecular structures shown in Fig. 2f. Although several non-ether compounds, such as amines, ketones, silyl ethers, and sulfonate esters (Fig. S8 and S9), were acquired in each batch, the AL framework may have developed a preference for ether solvents. This aligns with trends reported in the literature, where ether is the dominant solvent class to enable good anode-free cell cycling performance with single-solvent-single-salt and low concentration (~1 M) electrolytes^{12,13,35,40}. Fig. 2c shows the fraction of exclusive ether compounds (defined as any compound that contain C-O-C bonds but not any other functional groups, refer Supplementary Note 1) in the top 5000 or 10,000 suggestions from each batch. The fraction of total ether compounds fluctuates during initial batches and then steadily increases to around ~20% in batches 4 to 6, which is much higher than the fraction of ether compounds in the overall search space (2.5%) and hence confirms the preference towards ether solvents. In comparison, other functional group classes such as amides, even though are present in large fractions of the search space (Fig. S4a) and were initially suggested by the AL framework, could not be experimentally tested mainly due to their commercial unavailability. This occurred despite the initial screening of repositories using the synthesizability metric (Retro-synthetic Accessibility score; RAscore⁴¹), highlighting the limitations of such metrics in ensuring practical accessibility. We also evaluated the structural diversity of acquired molecules in different batches and similarity with respect to the in-house dataset through Wasserstein



distances, as shown in Fig. S11. The acquired molecules in the later batches become less diverse and chemically similar to the in-house dataset as the AL workflow progresses, due to the prominence of ether electrolytes similar to the in-house dataset (discussed in detail in Supplementary Note 8).

One possible origin of ether preference is the domination of ether solvents in the in-house dataset, as ~90% of them are ether-based

electrolytes. In the literature, ether solvents have also been investigated in a high fraction (about half) of all electrolytes reported for anode-free LMBs. However, the relative population of functional groups in batch 1 suggestions is similar to the search space (Fig. S4b), and no ether compound could be acquired from this pool of suggestions, indicating that ether preference is not attained immediately after training on the in-house data. Figure 2d shows the fraction of

Fig. 2 | Progress of AL suggestion and experimental acquisition and surrogate model interpretability. **a** 2D t-SNE plots depicting location of suggested molecules (denoted by different scatter shapes) on the virtual chemical search space across different batches. The virtual chemical space in the background has been colored according to different functional group classes. **b** Performance of electrolytes acquired in each batch. Electrolytes are tested in Cu||LFP cells and the discharge capacity at 20th cycle is used to compare performance. Capacity values are averaged from two replicated cells. The distribution and mean of performance in each batch is depicted by the vertical violin plots and square scatter points, respectively. **c** Fraction of exclusive ether molecules in the top suggestions in each batch. **d** Fraction of exclusive ether molecules in the molecules acquired from each batch. 'Batch 0' refers to the in-house dataset. **e** Fraction of common molecules in the top suggestions from pair of consecutive batches. **f** t-SNE plot depicting location of labeled electrolyte solvent molecules on the complete search space. Different colored scatter points indicate molecules acquired from the pool of top

suggested molecules in each batch. Only structures of the electrolyte solvent molecules having highest discharge capacity in each of the batches 2 to 6 and all top-performing molecules in the batch 7 are shown here for clarity. The green, orange, and red tick marks denote the presence of the three important molecular substructures predicted to be most relevant by the SHAP. The 7 best electrolyte solvent molecules identified by the AL framework appear in the two bottom rows below the t-SNE and are marked by purple stars shown after the discharge capacities in parentheses. **g** SHAP summary plot for C_{norm}^{20} prediction corresponding to rational quadratic (RQ) surrogate model obtained from batch 7. **h** Molecular substructures that contribute the most to the top molecular fingerprints predicted by SHAP towards C_{norm}^{20} prediction. **i** Fraction of all labeled molecules containing the three molecular substructures $-f_{sol}^6, f_{sol}^4, f_{sol}^5$ (left y-axis; refer Supplementary Note 10) and average C_{norm}^{20} (ground truth; $<C_{norm}^{20}>$) for electrolyte solvents containing these substructures (right y-axis). C_{norm}^{20} = normalized discharged capacity at 20th cycle.

ether molecules in each of the acquired batches, where the total ether fraction follows the same trend but is significantly higher than the total ether fraction in suggested molecules. This points towards another reason for ether preference – higher commercial availability of ethers compared to other compounds, since the first criterion for acquisition is the commercial availability itself. Moreover, Fig. 2d also shows less acquisition (fraction of molecules that were purchased/synthesized) of fluorinated ethers despite their consistent increased suggestion in the later batches, which is also attributed to the limited commercial availability of fluorinated ethers. Therefore, the preference towards ether, especially nonfluorinated ether compounds, is likely developed by the combined effects of an ether-dominated in-house dataset, wider availability of nonfluorinated ether compounds, and better performance of acquired ether electrolytes compared to compounds with other functional groups.

On the other hand, Fig. 2e shows that the fraction of suggested molecules common between successive batches increases gradually in the later batches. Specifically, over 60% of the top 5000 suggestions between batches 6 and 7 are unchanged, which indicates that the most promising region for anode-free LMBs has been identified by the AL framework after training with about 60 additional data points in 6 batches. The t-SNE plot shown in Fig. 2f also indicates clustering of top-performing acquired molecules from later batches in the middle and bottom-right corner. Since most commercially available compounds have been tested in the preceding batches and removed from the unlabeled dataset, only 3 commercially available compounds (7-1 to 7-3) are found within the top 5000 suggestions in batch 7. Therefore, we transitioned from EL-guided acquisition to greedy sampling (i.e., selecting candidates with high predicted values disregarding uncertainty) and ranked the suggestions according to their predicted performance (Supplementary Note 9). From the top 300 greedy sampling list, 6 compounds (7-11 to 7-16) are selected and tested according to synthesizability (synthesizable in one-step reaction from affordable precursors). As shown in Table S3, 5 out of the 9 molecules in batch 7 show relatively good performance in Cu||LFP cells with discharge capacity over 100 mAh/g at the 20th cycle. Batch 7 has also attained optimal performance, surpassing not only all preceding batches but also the in-house dataset, as shown by the distribution densities in Fig. S12. Specifically, batch 7 exhibits the lowest density at 0 capacity and a rightmost shift in high-capacity distribution compared to other batches and the in-house dataset. Including 6-3 and 5-7, a total of seven best-performing electrolyte solvents are identified in a single study (molecular structures shown in Fig. 2f marked with stars) – surpassing the combined contributions of multiple studies from any previous year (Fig. S13). Among them, 7-16, 7-14 and 7-12 have not been previously reported as electrolytes; 7-15 has only been reported in a patent⁴² but is absent from peer-reviewed literature; 7-1 was reported in a previous work, where it was only tested as a co-solvent for EC based electrolyte⁴³. 6-3 and 5-7 has been investigated as electrolytes for LIBs

and LMBs but no anode-free LMB performance has yet been reported^{44–48}. This indicates our AL framework can successfully filter out promising new electrolyte candidate and can accelerate the discovery of electrolytes relevant for anode-free LMBs even under data-scarcity limitations. Among the best performing electrolytes, 6-3, 7-1, 7-15 and 7-16 were selected for further investigation since they exhibit the best performance at 1 M LiFSA concentration. This selection is also balanced well in terms of fluorinated/nonfluorinated ethers and purchased/synthesized compounds.

Moreover, we applied SHAP (SHapley Additive exPlanations) analysis to evaluate whether the surrogate model in the AL framework learns meaningful, physically consistent trends. Post batch 7 training, SHAP analysis identified solvent molecular weight (MW_{sol}) as the most significant feature (Fig. 2g and S14a), alongside solvent fingerprints (f_{sol}^4, f_{sol}^5 , and f_{sol}^6 ; Fig. 2h) linked to molecular substructures such as methoxy, trifunctional, and tetrafunctional carbon centers respectively, which are prevalent in high-performing electrolytes (Fig. 2h). Importantly, the SHAP feature rankings align with trends observed in experimental performance, suggesting the model captures genuine feature-property relationships rather than dataset frequency effects (Fig. 2i). For instance, although the tetrafunctional molecular substructure is present in only about 20% of all tested electrolyte solvent molecules (listed in Table S3), it leads to the highest average normalized discharge capacity among the three identified substructures. The presence of these substructures is also indicated in the molecules shown in the t-SNE plot in Fig. 2f through tick marks in different colors. Further SHAP analyses for the relevant molecular fingerprints are shown in Fig. S14 and discussed in detail in Supplementary Note 10. However, SHAP results should be interpreted cautiously, as the method assumes feature independence and may overlook complex interactions or confounding effects, limiting its ability to fully capture the nuances of molecular design.

Cycling performance of AL-discovered electrolytes

To investigate lithium metal cycling performance, the four best AL-discovered electrolytes were tested in anode-free full cells and Li||Cu half cells. As shown in Fig. 3a, the best performing electrolytes in batches 6 and 7 (6-3, 7-1, 7-15, and 7-16 paired with 1 M LiFSA) all show stable capacity retention and high CE in anode-free Cu||LFP cells. 6-3 shows slightly higher initial capacity but collapses to the capacity of other electrolytes at later cycling. Figure 3b shows the discharge capacity normalized to the 1st C/3 (1 C = 150 mA g⁻¹) cycle capacity (3rd cycle) to eliminate the effect of initial capacity differences, where all good performing electrolytes have almost the same capacity retention curves. Compared to 4 M LiFSA in 1,2-dimethoxy ethane (DME), a high concentration electrolyte widely studied in LMBs^{49,50}, the AL-discovered electrolytes show higher initial capacity and better capacity retention. To calibrate cycling performance to state-of-the-art anode-free LMB electrolytes, a previously reported fluorinated ether

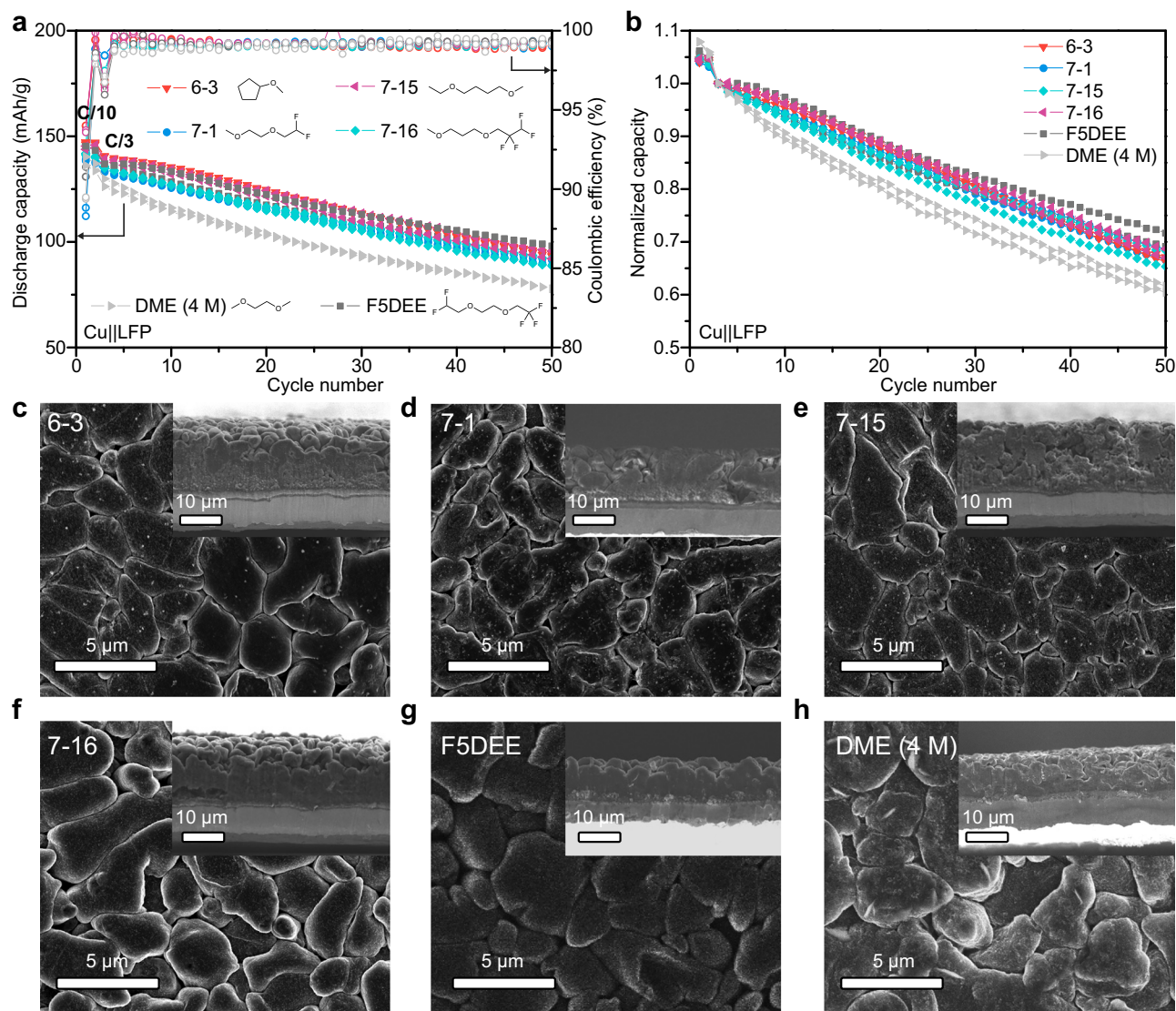


Fig. 3 | Performance of AL-discovered electrolytes. a Cycling performance of Cu||LFP cells at 20 °C using AL discovered electrolytes with 1 M LiFSA in F5DEE and 4 M LiFSA in DME as controls. 1 C = 150 mA g⁻¹. **b** Normalized discharge capacity of Cu||LFP cells at 20 °C using AL discovered electrolytes with 1 M LiFSA in F5DEE and 4 M LiFSA in DME as controls. Two replicated cells are shown for each electrolyte.

SEM images of lithium metal deposited in (c) 1 M LiFSA in 6-3, **d** 1 M LiFSA in 7-1, **e** 1 M LiFSA in 7-15, **f** 1 M LiFSA in 7-16, **g** 1 M LiFSA in F5DEE and **h** 4 M LiFSA in DME using Li||Cu cells with a current density of 1 mA cm⁻² to a capacity of 1.5 mAh cm⁻². The inset shows corresponding cross section SEM images of lithium metal sample.

solvent, 2-[2-(2,2-difluoroethoxy)ethoxy]-1,1,1-trifluoroethane (F5DEE) is selected as baseline¹³. Figure 3a, b shows that AL-discovered electrolytes have comparable cycling performance as the F5DEE control electrolyte. We do notice that the performance of Cu||LFP coin cells using 1 M LiFSA in F5DEE electrolyte in this study is not as good as literature reported Cu||LFP pouch cells. Such differences should be attributed to the much higher stack pressure of pouch cell⁵¹, the slow activation in pouch cell (indicated by increasing capacity in the initial cycles), and different discharging current rate. Significantly, it is important to note that while the four compounds are distinct (cyclic, linear nonfluorinated ether, highly fluorinated ether, medium fluorination), they reveal similar cycling behavior, showcasing the importance of the AL approach in navigating a wide electrolyte solvent chemical space.

The lithium metal compatibility of our best electrolytes obtained from AL framework was also evaluated by lithium metal deposition morphology. Figure 3c-h shows SEM images of lithium metal deposited in Li||Cu cell at 1 mA cm⁻² to 1.5 mAh cm⁻², where all four AL-discovered electrolytes lead to similar morphology with micron scale

granules in compact and uniform stacking. Such morphology is similar to the F5DEE and DME (4 M) control electrolytes and has been widely reported as evidence of good lithium metal compatibility and high lithium cycling efficiency in literature^{3,10,13,52,53}. Therefore, the desired lithium deposition morphology of AL-discovered electrolytes corroborates their high CE in anode-free LMB cycling.

While the AL framework was designed only for optimizing capacity retention in anode-free LMBs, the relatively large number and structural diversity of the AL discovered electrolytes may enable potential benefits in other performance metrics. For example, the rate capability test shown in Fig. S15a reveals that some AL-discovered electrolytes (7-1 and 6-3) have better rate capability (up to 2 C cycling) than the F5DEE control in Li||LFP cells. Preliminary tests were also conducted to probe low-temperature performance. Fig. S15b shows that some AL-discovered electrolytes (6-3 and 7-15) can support C/2 cycling of Li||LFP cells at -20 °C, which is also better than the F5DEE control. In the meantime, we must note that not all four AL-discovered electrolytes show optimal performance in the above-mentioned tests (7-16, for example). Future screening with additional target properties

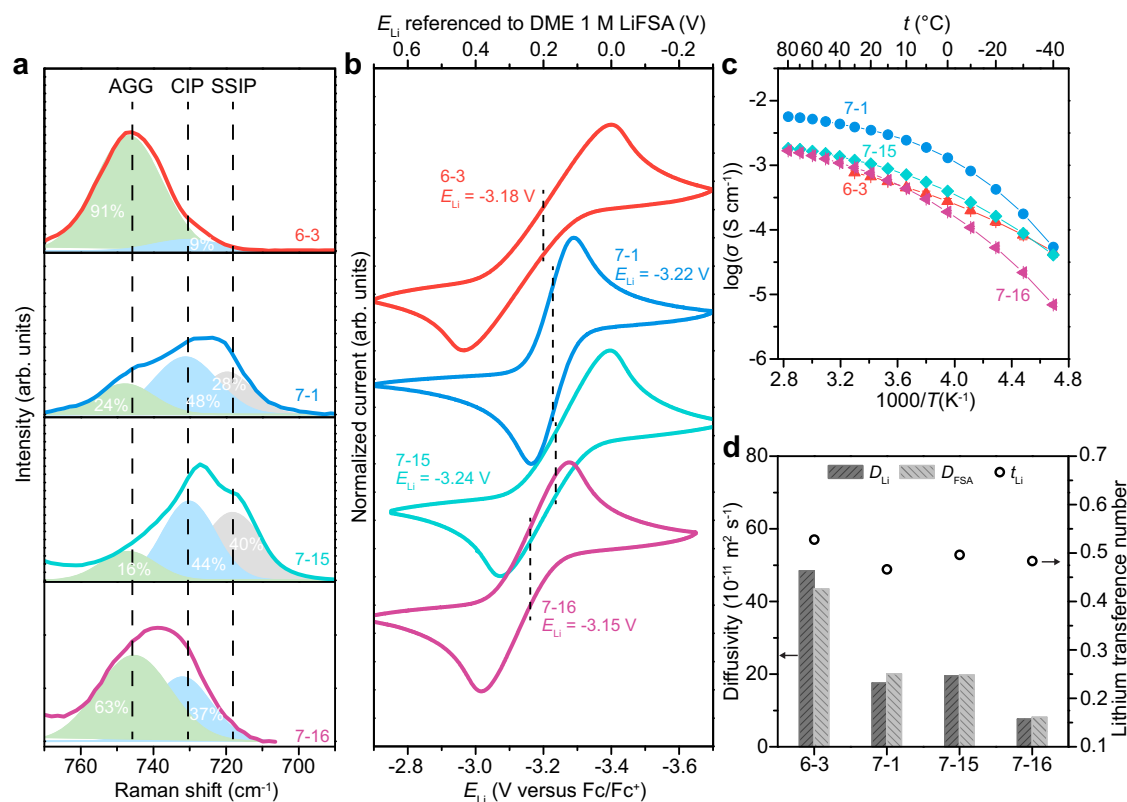


Fig. 4 | Ion solvation structure and ion transport. **a** Raman peak of FSA anion in AL discovered electrolytes at 1 M LiFSA concentration. SSIP: solvent separated ion pair; CIP: contact ion pair; AGG: salt aggregates. **b** Lithium redox potential (E_{Li} referenced to Fc/Fc^+) in AL discovered electrolytes at 1 M LiFSA concentration measured at room temperature ($25 \pm 2^\circ\text{C}$). **c** Ionic conductivity of 1 M LiFSA in AL-

discovered solvents as a function of temperature. Error bars represent standard deviation of three replicates. Lines are shown to guide the eyes. **d** Diffusivity of lithium ion (D_{Li}) and FSA anion (D_{FSA}) and lithium transference number (t_{Li}) of AL discovered electrolytes at 1 M LiFSA concentration.

will be needed to optimize electrolytes that satisfy the multi-objective requirements for practical applications.

Solvation structure and SEI properties

Ion solvation structure of AL-discovered electrolytes was investigated by spectroscopy and electrochemical techniques. Figure 4a shows the Raman peak of FSA anion in 1 M LiFSA electrolyte solutions. The fraction of different solvation environments can be estimated by deconvoluting FSA peak with three components: solvent-separated ion pair (SSIP); contact-ion pair (CIP) and salt aggregates (AGG)⁵⁴. All the AL-discovered electrolytes show high fractions of CIP and AGG (60–100% combining CIP and AGG), indicating their solvation structure is dominated by ion pairing. Interestingly, 6-3 and 7-16 lead to especially high AGG fractions of 91% and 63%, respectively, which matches with that of high concentration electrolytes widely known for strong salt aggregation^{54–56}. In comparison, 7-1 and 7-15 have less AGG but more CIP fraction of over 40%. Figure 4b shows Li/Li^+ potentials (E_{Li}) reference to ferrocene (Fc/Fc^+) measured by the protocol recently reported by Yamada et al.⁵⁷. Compared to well solvated electrolytes such as 1 M LiFSA in DME ($E_{Li} = -3.40$ V), the higher E_{Li} (less reductive potentials) of AL discovered electrolytes suggest weaker Li^+ coordinating environment and more ion pairing. Among them, 6-3 ($E_{Li} = -3.18$ V) and 7-16 ($E_{Li} = -3.15$ V) have higher E_{Li} than 7-1 ($E_{Li} = -3.22$ V) and 7-15 ($E_{Li} = -3.24$ V), which agrees with the trend observed in Raman spectroscopy. As summarized in Fig. S16, the degree of ion pairing in 6-3 and 7-16 is comparable to F5DEE while 7-1, 7-15 and DME (4 M) electrolytes show relatively less ion pairing. However, the correlation between solvation structure descriptors and anode-free LMB performance remains unclear among the electrolytes under investigation. This is likely due to the subtle performance differences and suggests

that increasing ion pairing beyond a certain threshold does not necessarily lead to better lithium metal cycling performance^{13,36,57}. The ion transport properties of AL-discovered electrolytes were also studied. Figure 4c shows the ionic conductivity of 6-3, 7-1, 7-15 and 7-16 with 1 M LiFSA measured by electrochemical impedance spectroscopy (EIS). At 20°C , 7-1 electrolyte has the highest ionic conductivity of 3.5 mS/cm and the other three electrolytes show acceptable conductivities of 0.7–1.0 mS/cm. While the room temperature conductivity is lower than those reported for control electrolytes (5.0 mS/cm for 1.2 M LiFSA in F5DEE¹³ and 5.7 mS/cm for 4 M LiFSA in DME⁴⁹), some of AL-discovered electrolytes do show appreciable rate performance as discussed earlier (Fig. S15). Figure 4d shows the ion diffusivity and lithium transference number of AL-discovered electrolytes measured by pulsed field gradient nuclear magnetic resonance (PFG NMR), where the ion diffusivities in general decrease with increasing viscosity (Table S5) from 6-3 to 7-16. While the AL-discovered electrolytes show lower ionic conductivity, the lithium ion diffusivity (D_{Li}) of 6-3, 7-1, and 7-15 is higher than F5DEE ($D_{Li} = 9.28 \times 10^{-11}$ m²/s) or DME (4 M) ($D_{Li} = 3.96 \times 10^{-11}$ m²/s) controls, which indicates ionic conductivity is also affected by the concentration of free charge carriers. All four AL-discovered electrolytes show high lithium transference number ranging from 0.47 to 0.53, which is similar to the control electrolytes (0.49 for F5DEE and 0.47 for DME (4 M)) and agrees with the solvation structure rich in ion pairing as discussed earlier.

Solid electrolyte interphase (SEI) composition from AL-discovered electrolytes was investigated by X-ray photoelectron spectroscopy (XPS) and compared to control electrolytes. Figure 5a shows that AL-discovered electrolytes produce a similar pattern of F 1s XPS spectra, where a small amount of LiF is found on the surface of SEI and more LiF is revealed in the inner layers with etching. In the O 1s

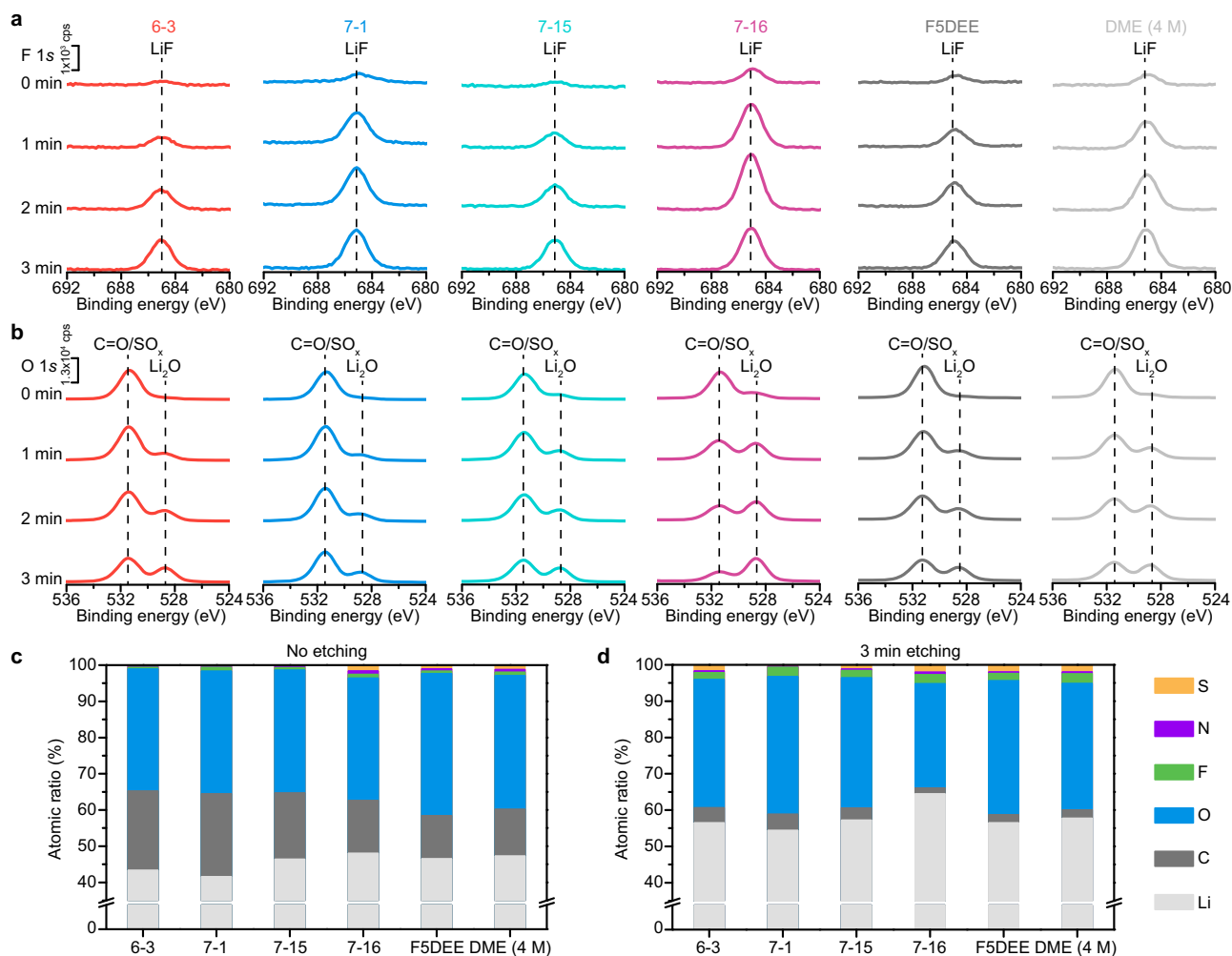


Fig. 5 | SEI composition. **a** F 1s XPS spectra of lithium metal SEI at different etching time. **b** O 1s XPS spectra of lithium metal SEI at different etching time. Atomic ratio quantified from XPS with **(c)** no etching and **(d)** 3 minutes of etching.

XPS spectra shown in Fig. 5b, all AL-discovered electrolytes have a main peak for carbonate/SO_x species and a small amount of Li₂O on the surface layer of SEI. With etching, the carbonate/SO_x peak reduces, and the fraction of Li₂O increases. Fig. S17 shows C 1s XPS spectra, where the carbon peak is strong at the surface but decreases significantly after 30 seconds of etching. This indicates organic species are concentrated at the surface layer of the SEI. Figure 5c, d show the atomic ratio of each element quantified by XPS. Before etching, carbon (from organic species) and oxygen (mainly from carbonate/SO_x species) have a high fraction at the surface layer of SEI. After 3 minutes of etching, the increased atomic ratio of fluorine, sulfur, and oxygen indicates the inner layer of SEI contains more inorganic components such as LiF, Li₂O, Li₂CO₃ and Li₂S_x. Compared to F5DEE and DME (4 M) control electrolytes, AL-discovered electrolytes show similar SEI compositions and depth profiles. Such SEI structure resembles the anion-derived inorganic-rich SEI widely reported for electrolytes with good lithium metal compatibility^{13,53,58}.

Discussion

In this work, we demonstrated an AL framework for accelerating electrolyte discovery for anode-free lithium metal batteries, starting with a small in-house dataset of 58 electrolytes. Using BMA over GPs with different covariance kernels and a virtual search space of 1 million candidates, our AL workflow efficiently identified optimal electrolytes based on capacity retention in Cu || LFP cells. Over six iterative batches, the model consistently favored ether solvents, and subsequent

synthesis and testing revealed four electrolytes with cycling performance that rival state-of-the-art systems. Therefore, our “parameter-free” AL approach effectively correlated electrolyte composition with battery performance. Additionally, analysis of solvation structures and SEI composition revealed similarities to high-performing electrolytes reported in the literature, confirming the validity of our approach.

However, several limitations must be acknowledged. First, all experimental validations for AL suggestions were conducted using Cu || LFP cells, which, while widely used for laboratory-scale evaluation, do not encompass the high-voltage positive electrodes (e.g., NMC811) that are also of great interest. Additionally, our study was limited to a single solvent and a single lithium salt (LiFSA) at a fixed 1 M concentration, which does not make use of formulation strategies well developed in the electrolyte literature. Therefore, the use of alternative salts, higher salt concentration additives, and diluents may further enhance interphase stability and cycle life. Another limitation is the practical accessibility of identified solvents. The AL framework prioritized purchasable molecules to accelerate the discovery process; however, many high-ranking candidates were unavailable commercially. While we successfully synthesized several promising candidates, future studies could integrate predictive models for solvent synthesizability and salt solubility to further refine selection criteria. Additionally, our study optimized capacity retention as a single target. While capacity retention might be the bottleneck for commercializing anode-free LMBs, practical battery applications also demand other properties such as rate capability, working temperature window, and safety. Expanding the AL framework to a

multi-objective optimization paradigm would make electrolyte optimization more relevant to real-world applications.

Despite these limitations, this study establishes a robust foundation for AI-driven electrolyte discovery. The demonstrated AL workflow can be extended to other battery chemistries and integrated with automated experimental workflows for high-throughput screening. As ML techniques continue to evolve, combining AL with self-driving laboratories and multi-objective optimization has the potential to revolutionize battery research, accelerating the materials development for next-generation energy storage technologies.

Methods

Data analysis and AL setup

To accelerate electrolyte discovery for anode-free lithium metal batteries (LMBs), we employed an AL framework that iteratively refines predictions based on sequential experimental feedback. The AL workflow consists of the following steps:

Creation of virtual search space. The initial chemical search space (~1 million electrolytes) was constructed using small organic molecules filtered from eMolecules and PubChem databases. Molecules with undesirable functional groups (e.g., radicals, nitriles, aromatics) or low synthetic accessibility (RAscore <0.01) were removed, resulting in ~380,000 unique solvent molecules for AL-driven optimization. Further details are provided in Supplementary Note 1.

Feature representation and model training. Molecular structures were represented using 1024-bit Morgan fingerprints (ECFP4), which were dimensionally reduced to 10 components via principal component analysis (PCA) to enhance computational efficiency for GP models. Other input features included salt identity, salt concentration, and electrolyte composition. The surrogate models were trained using GPR with four different covariance kernels: Radial Basis Function (RBF) + Exponential Sine Squared (ESS), Matern-3/2, Rational Quadratic (RQ), and Pairwise Kernels. Bayesian model averaging (BMA) was applied to integrate predictions from all four GP models, balancing their strengths and improving uncertainty estimation. Further details are provided in Supplementary Notes 2, 3, and 5.

Acquisition strategy using expected improvement (EI). The trained surrogate models generated predicted means and uncertainties for the unlabeled search space, and molecules were ranked based on their EI scores. The aggregated EI (EI^{agg}) was computed using weighted model predictions from BMA, guiding the selection of molecules for experimental testing. Further details are provided in Supplementary Note 6.

Sequential batch selection and search space evolution. In each batch, top-ranked solvent molecules (based on EI^{agg}) were experimentally tested in Cu||LFP coin cells with 1 M LiFSA. Tested molecules were permanently removed from the search space before the next iteration to ensure non-redundant selection. Initial batches prioritized exploration (diverse functional groups such as amides, amines, imides), while later batches shifted toward exploitation (predominantly ether-based solvents) as the model refined its predictions.

Experimental feedback and model refinement. Battery cycling performance (normalized discharge capacity at 20th cycle, C_{norm}^{20}) was measured and added to the training dataset. The AL loop was repeated across six batches, refining predictions in each iteration until model convergence was observed. Further details are provided in Supplementary Note 2.

Computational implementation. All codes utilized in this study were built using various libraries available in the Python (version 3.9.12)

programming language. Morgan fingerprints used for representing molecules for training surrogate models and for t-SNE visualization were generated using the RDKit library. The Scikit-learn (version 0.23) library was employed for standardizing datasets, training the GPs using different covariance kernels (detailed explanation in Supplementary Note 5), and calculating error metrics. The reduced embeddings of chemical space for the t-SNE plots were generated using the OpenTSNE library. The numpy and scipy libraries were used for performing most numerical analyses, such as Wasserstein distances, cumulative and probability distribution functions (for calculating EI). All plots in the manuscript were made using matplotlib, seaborn, or plotly libraries in Python or Origin.

Materials

Commercially available electrolyte solvents were purchased from sources listed in Table S3. $MgSO_4$ (anhydrous, 97%), N-methyl-2-pyrrolidone (NMP, 99%), NaH (60 wt% separated in mineral oil), KOH powder (synthesis grade), diethyl ether ($\geq 99.9\%$, inhibitor-free), and 4 Å molecular sieves were purchased from Sigma-Aldrich. 3-Methoxy-1-propanol (97%), 4-methoxy-1-butanol (98%), 2,2,3,3-tetrafluoropropyl tosylate (97%), 1-bromo-2,2-dimethylpropane (98%), 1-bromo-2-(2-methoxyethoxy)ethane (90%, stabilized with Na_2CO_3), 1-bromo-3-methoxypropane (98%), and tetraethylene glycol dimethyl ether (tetraglyme, 97%) were purchased from AmBeed. Tetrahydrofuran (THF, certified grade, stabilized with BHT), ethyl p-toluenesulfonate (98%), 1-iodobutane (98%, stabilized with copper), 2-methoxyethyl methylamine (97%), triethyl amine (99%), ethyl acetate (EA, $\geq 99.9\%$), and hexane ($\geq 98.5\%$) were purchased from Fisher Scientific. Lithium bis(fluorosulfonyl) amide (LiFSA, 99%) was purchased from Arkema. Deuterated solvents (≥ 99.8 atom% D) were purchased from Cambridge Isotope Laboratories.

We purchased Celgard 2325 separator (25 μm thickness and 39% porosity) from Celgard LLC. We then cut the Celgard 2325 separator into 18 mm diameter disks, rinsed with acetone three times, and then vacuum dried it overnight at 70 °C in a BUCHI B-585 glass oven before transferring into the argon glovebox without air exposure. We purchased all CR2032 coin cell parts from Xiamen TOB New Energy Technology, except for lithium foil (500 μm thick), which was purchased from China Energy Lithium. We also polished the lithium foil with a brush to remove any oxide layer and later cut it into 12 mm diameter disks before use. The LFP, NMC811, and NMC111 ($LiNi_{0.33}Mn_{0.33}Co_{0.33}O_2$) electrodes were procured from Cell Analysis, Modeling, and Prototyping (CAMP) facility in the Argonne National Laboratory. The specifications of the electrode can be found in Table S4 in the SI. The electrodes were cut into 12 mm diameter disks inside an argon-filled glovebox (O_2 , H_2O <1ppm) and vacuum dried in a heated antechamber of the glovebox at 120 °C before use. We dried all solvents investigated in the present study using 4 Å molecular sieves overnight inside the argon glovebox. The LiFSA salt was vacuum dried at 120 °C overnight in a heated glovebox antechamber prior to use and was prevented from air exposure at all times. We used all other chemicals as received.

Synthesis

Synthesis of 3-6, 7-11, and 7-12. For synthesizing 7-12, we added 150 mL dry tetraglyme to a round-bottom flask, followed by 2.4 g (1.1 eq.) NaH (60 wt% separated in mineral oil) under stirring and nitrogen atmosphere. We then cooled the suspension to 0 °C with an ice bath, and added 5.6 g (1.0 eq.) 4-methoxy-1-butanol dropwise. We stirred the mixture thus obtained for 2 hours while slowly increasing the temperature from 0 °C to room temperature. Then, we slowly added a solution containing 13.7 g (1.0 eq.) 2,2,2-trifluoroethyl p-toluenesulfonate and 10 mL dry tetraglyme to the reaction flask at 0 °C. The flask was subsequently heated slowly to 70 °C. After an overnight reaction at 70 °C, we directly distilled out the crude product from the reaction mixture at reduced pressure. The distillation was

repeated with a small amount of NaH at ~5 mbar (b.p. -34 °C), resulting in 3.3 g (33% yield) pure product as a colorless liquid. 7-11 was obtained from the reaction between 3-methoxy-1-propanol and 1-bromo-2,2-dimethylpropane with 14% yield following the same procedure, except the reaction was kept at 160 °C overnight. 3-6 was obtained from the reaction between 2,2,3,3-tetrafluoro-1-propanol and 1-bromo-2-(2-methoxyethoxy) ethane with 53% yield following a similar procedure except for THF being used as solvent instead of tetraglyme. Then THF was removed under vacuum before the first distillation.

Synthesis of 7-14, 7-15, and 7-16. For synthesizing 7-15, we added 10.9 g (1.0 eq.) 4-methoxy-1-butanol, 20 mL NMP, and 7.8 g (1.2 eq.) KOH powder to a round-bottom flask under an ice bath. Then, we added 21.0 g (1.0 eq.) ethyl p-toluenesulfonate dissolved in 20 mL NMP to the flask dropwise under an ice bath. We stirred the mixture thus obtained overnight and increased the temperature from 0 °C to room temperature. Subsequently, 75 mL ice water was added to the flask, followed by the addition of 75 mL diethyl ether. The organic layer was separated, first washed with 50 mL Milli-Q water twice and then with 50 mL brine once. It was then dried with anhydrous MgSO₄ and the diethyl ether was removed by rotary evaporation. The remaining product was purified by flash column chromatography (BUCHI, EA/hexane, 0–30 EA vol.%). The crude product was then distilled at -15 mbar (b.p. -42 °C), resulting in 4.7 g (34% yield) pure product as a colorless liquid. 7-14 was obtained from the reaction between 3-methoxy-1-propanol and 1-iodobutane with 37% yield following the same procedure. 7-16 was obtained from the reaction between 3-methoxy-1-propanol and 2,2,3,3-tetrafluoropropyl tosylate with 48% yield following the same procedure.

Synthesis of 3-7. 5.3 g (1.0 eq.) 2-Methoxyethyl methylamine, 6.7 g (1.1 eq.) triethylamine, and 250 mL dry dichloromethane was added to a round-bottom flask under nitrogen protection. The solution was cooled down to -10 °C by a NaCl/ice bath, and 6.9 g (1.0 eq.) methyl sulfonyl chloride was added dropwise. After stirring at room temperature overnight, the mixture was washed with 150 mL 2 M hydrochloric acid twice, 150 mL water once, and 150 mL brine once. The organic phase was dried over anhydrous MgSO₄ and concentrated. The remaining solution was distilled at ~2 mbar (b.p. -54 °C) to receive 5.6 g (56% yield) pure product as a colorless liquid.

Synthesis of 7-13. To a round-bottom flask was added 24.9 g (1.0 eq.) 1-bromo-3-methoxypropane, 56.5 g (1.1 eq.) TBAF·3H₂O and 50 mL tetraglyme. The mixture was heated up to 70 °C to form a pale yellow solution. After reacting at 70 °C overnight, crude product was directly distilled out in a mixture with water under reduced pressure (300 mbar). NaCl was added to the mixture to saturate the aqueous phase, and the organic layer was extracted. The organic layer was washed with 2 mL 30 wt% sulfuric acid twice and 2 mL brine twice. Then the remaining organic layer was dried over anhydrous MgSO₄, filtered through a syringe filter, and fractional distillation was performed (b.p. -80 °C) to receive 0.43 g (3% yield) pure product as a colorless liquid.

Physical characterization

Nuclear magnetic resonance (NMR) spectroscopy. We performed NMR spectroscopy for all synthesized products on a Bruker Ascend 9.4 T/400 MHz instrument. To prepare samples for NMR, several milligrams of the synthesized product was dissolved into 0.5 mL CDCl₃. A Bruker Ultrashield Plus 11.7 T / 500 MHz instrument was used to perform pulsed-field gradient (PFG) NMR. To prepare an electrolyte NMR sample, around 0.5 mL of deuterated acetonitrile was added to an NMR tube (Wilmad) and the capillary tube with sealed electrolyte was inserted. The NMR tube was capped and sealed using parafilm inside the glovebox. The PFG NMR experiment was performed using pulse sequence “ledgp2s”, with gradient strengths up to 48 G/cm, pulses of

$\delta = 4.2$ ms, and gradient pulse intervals of 0.5–1 s. Diffusion constants were obtained by fitting the following equation:

$$I = I_0 e^{-\gamma^2 g^2 \delta^2 D (\Delta - \frac{\delta}{3})}$$

where I = peak area (as a function of gradient), γ = gyromagnetic ratio, g = gradient strength, D = diffusion constant, Δ = gradient pulse interval, and δ = pulse duration.

Raman spectroscopy. A Raman sample was prepared by sealing 7 μ L electrolyte in a glass chamber built with glass slides (Chemglass Life Science) and silicone isolators (Grace Bio-Labs) inside an argon-filled glovebox. Raman spectra were collected with a HORIBA LabRAM HR Evolution Confocal Raman Microscope with a 532 nm ULF laser as light source.

Scanning electron microscopy (SEM) and X-ray photoelectron spectroscopy (XPS). We prepared lithium metal samples for SEM and XPS by depositing lithium metal on Cu in Li||Cu coin cell at 1 mA cm⁻² to 1.5 mAh cm⁻². The Li on Cu sample was retrieved by disassembling the prepared coin cell inside an argon glovebox. The sample was rinsed with anhydrous DME three times, and dried under vacuum at room temperature (25 ± 2 °C) before testing. A Carl Zeiss Merlin Field Emission Scanning Electron Microscope was used to perform SEM on lithium metal sample. The samples were cut with a doctor blade for carrying out cross-sectional SEM. A ThermoFisher Scientific XPS: NEXSA G2 instrument was used for performing XPS and an EX06 monatomic Ar ion source was used for performing etching. The lithium metal sample was transferred from glovebox to the XPS instrument using an air-tight chamber to prevent air exposure.

Electrochemical characterizations

Coin cell preparation. All coin cells were assembled inside an argon-filled glovebox (O₂, H₂O <1 ppm). Li||Cu cells were prepared in the following configuration: negative case | conical spring | spacer | Li | 25 μ L electrolyte | separator | 25 μ L electrolyte | Cu | spacer | positive case. Cu||LFP cells were prepared in the following configuration: negative case | conical spring | spacer | spacer | Cu | 25 μ L electrolyte | separator | 25 μ L electrolyte | LFP | spacer | positive case. Cu||NMC (NMC811 or NMC111) cells were prepared in the following configuration: negative case | conical spring | spacer | spacer | Cu | 25 μ L electrolyte | separator | 25 μ L electrolyte | NMC | Al foil | Al-coated positive case. Stainless steel || stainless steel (SS || SS) cells were prepared in the following configuration: negative case | wave spring | spacer | 25 μ L electrolyte | separator | 25 μ L electrolyte | spacer | positive case.

General coin cell tests. All coin cell cycling were performed inside a temperature-controlled room at 20 ± 1 °C unless specified separately. Low temperature cycling of coin cells was performed inside an ESPEC environmental chamber (BTZ-133), with temperature control accuracy of ± 0.1 °C. Cu||LFP cells were cycled in a voltage window of 2.9–3.8 V. Cu||NMC111 cells were cycled in a voltage window of 3–4.3 V. Cu||NMC811 cells were cycled in a voltage window of 3–4.4 V. Two formation cycles were performed at a current rate of C/10 before long-term cycling at C/3 (1C = 150 mA g⁻¹, 161 mA g⁻¹, and 203 mA g⁻¹ for LFP, NMC111, and NMC811 positive electrodes, respectively).

Electrochemical impedance spectroscopy (EIS). SS||SS cells were tested inside an ESPEC environmental chamber (BTZ-133). Temperature was first set to 80 °C and cooled in 10 degree intervals to -60 °C (or 30 °C to -60 °C for 6-3) while holding at each temperature for 1 hour before EIS measurement. A Biologic VSP-300 Potentiostat was used to collect impedance spectra at open-circuit voltage with 10 mV single-sine signal between 7 MHz and 100 Hz under sampling conditions of 10 points per decade. A cell constant of 12.4 was calibrated by a

Platinum-Cell Conductivity Probe (Vernier) using E3F1 1 M LiFSA solution at 25 °C^{59,60}.

Lithium potential tests. We performed the lithium potential tests using Li||Pt micro beaker cells inside an argon-filled glovebox (O₂, H₂O <1ppm) at room temperature (−25 °C). The micro beaker cell was prepared using a platinum wire as the working electrode and a lithium wire as both counter and reference electrodes. The electrodes were immersed in a 2 mL glass vial containing 200 µL of given electrolyte with 1 mM ferrocene. Three cyclic voltammetry (CV) scans were performed at a scan rate of 5 mV/s (oxidation first), and the second scan was used for calculating the lithium potential.

Data availability

All experimental cycling data can be found in the Supporting Information and on the accompanying GitHub repository. Source data are provided with this paper.

Code availability

The Jupyter notebooks and model checkpoints have been made publicly available on GitHub repository under MIT open source license (<https://github.com/AmanchukwuLab/AL-anode-free>)⁶¹.

References

- Schmich, R., Wagner, R., Hörpel, G., Placke, T. & Winter, M. Performance and cost of materials for lithium-based rechargeable automotive batteries. *Nat. Energy* **3**, 267–278 (2018).
- Lin, D., Liu, Y. & Cui, Y. Reviving the lithium metal anode for high-energy batteries. *Nat. Nanotechnol.* **12**, 194–206 (2017).
- Louli, A. J. et al. Diagnosing and correcting anode-free cell failure via electrolyte and morphological analysis. *Nat. Energy* **5**, 693–702 (2020).
- Nanda, S., Gupta, A. & Manthiram, A. Anode-free full cells: a pathway to high-energy density lithium-metal batteries. *Adv. Energy Mater.* **11**, 2000804 (2021).
- Niu, C. et al. Balancing interfacial reactions to achieve long cycle life in high-energy lithium metal batteries. *Nat. Energy* **6**, 723–732 (2021).
- Xiao, J. et al. Understanding and applying coulombic efficiency in lithium metal batteries. *Nat. Energy* **5**, 561–568 (2020).
- Cao, X. et al. Monolithic solid–electrolyte interphases formed in fluorinated orthoformate-based electrolytes minimize Li depletion and pulverization. *Nat. Energy* **4**, 796–805 (2019).
- Zewen, Z. et al. Capturing the swelling of solid-electrolyte interphase in lithium metal batteries. *Science* (80-) **375**, 66–70 (2022).
- Hobold, G. M.; Kim, K.-H.; Gallant, B. M. Beneficial vs. Inhibiting Passivation by the Native Lithium Solid Electrolyte Interphase Revealed by Electrochemical Li⁺ Exchange. *Energy Environ. Sci.* <https://doi.org/10.1039/D2EE04203G> (2023).
- Ren, X. et al. Enabling high-voltage lithium-metal batteries under practical conditions. *Joule* **3**, 1662–1676 (2019).
- Weber, R. et al. Long cycle life and dendrite-free lithium morphology in anode-free lithium pouch cells enabled by a dual-salt liquid electrolyte. *Nat. Energy* **4**, 683–689 (2019).
- Yu, Z. et al. Molecular design for electrolyte solvents enabling energy-dense and long-cycling lithium metal batteries. *Nat. Energy* **5**, 526–533 (2020).
- Yu, Z. et al. Rational solvent molecule tuning for high-performance lithium metal battery electrolytes. *Nat. Energy* **7**, 94–106 (2022).
- Kumar, R. & Singh, A. K. Chemical hardness-driven interpretable machine learning approach for rapid search of photocatalysts. *npj Comput. Mater.* **7**, 197 (2021).
- Stokes, J. M. et al. A deep learning approach to antibiotic discovery. *Cell* **180**, 688–702.e13 (2020).
- Wong, F. et al. Discovery of a structural class of antibiotics with explainable deep learning. *Nature* **626**, 177–185 (2024).
- Kumar, R., Vu, M. C., Ma, P. & Amanchukwu, C. V. Electrolytics: A unified big data approach for electrolyte design and discovery. *Chem. Mater.* **37**, 2720–2734 (2025).
- Hie, B., Bryson, B. D. & Berger, B. Leveraging uncertainty in machine learning accelerates biological discovery and design. *Cell Syst.* **11**, 461–477.e9 (2020).
- Attia, P. M. et al. Closed-loop optimization of fast-charging protocols for batteries with machine learning. *Nature* **578**, 397–402 (2020).
- Ma, X.-Y., Zhang, W.-K., Yin, Y., Liu, K. & Yang, X.-G. Multi-objective optimization of lithium-ion battery designs considering the dilemma between energy density and rate capability. *Energy AI* **18**, 100416 (2024).
- Agarwal, G., Doan, H. A., Robertson, L. A., Zhang, L. & Assary, R. S. Discovery of energy storage molecular materials using quantum chemistry-guided multiobjective bayesian optimization. *Chem. Mater.* **33**, 8133–8144 (2021).
- Doan, H. A. et al. Quantum chemistry-informed active learning to accelerate the design and discovery of sustainable energy storage materials. *Chem. Mater.* **32**, 6338–6346 (2020).
- Lee, D. K. J., Tan, T. L. & Ng, M.-F. Machine learning-assisted Bayesian optimization for the discovery of effective additives for dendrite suppression in lithium metal batteries. *ACS Appl. Mater. Interfaces* **16**, 64364–64376 (2024).
- Dave, A. et al. Autonomous optimization of non-aqueous li-ion battery electrolytes via robotic experimentation and machine learning coupling. *Nat. Commun.* **13**, 5454 (2022).
- Zhu, S. et al. Differentiable modeling and optimization of non-aqueous Li-based battery electrolyte solutions using geometric deep learning. *Nat. Commun.* **15**, 8649 (2024).
- Noh, J. et al. An integrated high-throughput robotic platform and active learning approach for accelerated discovery of optimal electrolyte formulations. *Nat. Commun.* **15**, 2757 (2024).
- Talapatra, A. et al. Autonomous efficient experiment design for materials discovery with Bayesian model averaging. *Phys. Rev. Mater.* **2**, 113803 (2018).
- Mamun, O., Winther, K. T., Boes, J. R. & Bligaard, T. A Bayesian framework for adsorption energy prediction on bimetallic alloy catalysts. *npj Comput. Mater.* **6**, 177 (2020).
- Betz, J. et al. Cross talk between transition metal cathode and Li metal anode: unraveling its influence on the deposition/dissolution behavior and morphology of Lithium. *Adv. Energy Mater.* **9**, 1900574 (2019).
- Tan, S. et al. Unravelling the convoluted and dynamic interphasial mechanisms on Li metal anodes. *Nat. Nanotechnol.* **18**, 243–249 (2023).
- Kim, S. C. et al. Data-driven electrolyte design for lithium metal anodes. *Proc. Natl. Acad. Sci.* **120**, e2214357120 (2023).
- Sharma, V. et al. Formulation graphs for mapping structure-composition of battery electrolytes to device performance. *J. Chem. Inf. Model.* **63**, 6998–7010 (2023).
- Zeng, B. et al. Uni-ELF: A Multi-level representation learning framework for electrolyte formulation design. *arXiv preprint arXiv:2407.06152* (2024).
- Xue, D. et al. Accelerated search for materials with targeted properties by adaptive design. *Nat. Commun.* **7**, 11241 (2016).
- Zhang, G. et al. A monofluoride ether-based electrolyte solution for fast-charging and low-temperature non-aqueous lithium metal batteries. *Nat. Commun.* **14**, 1081 (2023).
- Wu, L.-Q. et al. Unveiling the role of fluorination in hexacyclic coordinated ether electrolytes for high-voltage lithium metal batteries. *J. Am. Chem. Soc.* **146**, 5964–5976 (2024).

37. Li, A.-M. et al. Methylation enables the use of fluorine-free ether electrolytes in high-voltage lithium metal batteries. *Nat. Chem.* **16**, 922–929 (2024).
38. Wolpert, D. H. & Macready, W. G. No free lunch theorems for optimization. *IEEE Trans. Evol. Comput.* **1**, 67–82 (1997).
39. Boobier, S., Hose, D. R. J., Blacker, A. J. & Nguyen, B. N. Machine learning with physicochemical relationships: solubility prediction in organic solvents and water. *Nat. Commun.* **11**, 5753 (2020).
40. Ma, P. et al. Probing the influence of steric hindrance in non-fluorinated ether electrolytes for lithium metal batteries. *J. Electrochem. Soc.* **171**, 120536 (2024).
41. Thakkar, A., Chadimová, V., Bjerrum, E. J., Engkvist, O. & Reymond, J.-L. Retrosynthetic Accessibility Score (RAscore) – rapid machine learned synthesizability classification from AI driven retrosynthetic planning. *Chem. Sci.* **12**, 3339–3349 (2021).
42. Lin, L. I.; Fengquan, L. I. U.; Jianjun, Z. Gelatinized System And Applications In Lithium Air Battery, Super Capacitor Or Capacitor Battery In Organic System, (2020).
43. Sasaki, Y., Shimazaki, G., Nanbu, N., Takehara, M. & Ue, M. Physical and electrolytic properties of partially fluorinated organic solvents and its application to secondary lithium batteries: partially fluorinated dialkoxyethanes. *ECS Trans.* **16**, 23–31 (2009).
44. Wang, Z. et al. Co-intercalation-free ether-based weakly solvating electrolytes enable fast-charging and wide-temperature lithium-ion batteries. *ACS Nano* **17**, 18103–18113 (2023).
45. Zhang, H. et al. Cyclopentylmethyl ether, a non-fluorinated, weakly solvating and wide temperature solvent for high-performance lithium metal battery. *Angew. Chem. Int. Ed.* **62**, e202300771 (2023).
46. Liang, J.-L. et al. Regulating the electrolyte solvation structure by weakening the solvating power of solvents for stable lithium metal batteries. *Sci. China Chem.* **66**, 3620–3627 (2023).
47. Chen, S. et al. Unveiling the critical role of ion coordination configuration of ether electrolytes for high voltage lithium metal batteries. *Angew. Chem. Int. Ed.* **62**, e202219310 (2023).
48. Wu, L.-Q. et al. Hexacyclic chelated lithium stable solvates for highly reversible cycling of high-voltage lithium metal battery. *ChemSusChem* **16**, e202300590 (2023).
49. Qian, J. et al. High rate and stable cycling of lithium metal anode. *Nat. Commun.* **6**, 6362 (2015).
50. Qian, J. et al. Anode-free rechargeable lithium metal batteries. *Adv. Funct. Mater.* **26**, 7094–7102 (2016).
51. Fang, C. et al. Pressure-tailored lithium deposition and dissolution in lithium metal batteries. *Nat. Energy* **6**, 987–994 (2021).
52. Fang, C. et al. Quantifying inactive lithium in lithium metal batteries. *Nature* **572**, 511–515 (2019).
53. Chen, Y. et al. Origin of Dendrite-free lithium deposition in concentrated electrolytes. *Nat. Commun.* **14**, 2655 (2023).
54. Wang, J. et al. Superconcentrated electrolytes for a high-voltage lithium-ion battery. *Nat. Commun.* **7**, 12032 (2016).
55. Xie, J.-D. et al. Highly concentrated carbonate electrolyte for Li-ion batteries with lithium metal and graphite anodes. *J. Power Sources* **450**, 227657 (2020).
56. Peng, Z. et al. High-power lithium metal batteries enabled by high-concentration Acetonitrile-based electrolytes with vinylene carbonate additive. *Adv. Funct. Mater.* **30**, 2001285 (2020).
57. Ko, S. et al. Electrode potential influences the reversibility of lithium-metal anodes. *Nat. Energy* **7**, 1217–1224 (2022).
58. Ruan, D. et al. Solvent versus anion chemistry: unveiling the structure-dependent reactivity in tailoring electrochemical interphases for lithium-metal batteries. *JACS Au*. <https://doi.org/10.1021/jacsau.3c00035> (2023).
59. Ma, P., Mirmira, P. & Amanchukwu, C. V. Effect of building block connectivity and ion solvation on electrochemical stability and ionic conductivity in novel fluoroether electrolytes. *ACS Cent. Sci.* **7**, 1232–1244 (2021).
60. Ma, P. et al. Molecular structure optimization of fluorinated ether electrolyte for all temperature fast charging lithium-ion battery. *ACS Energy Lett.* **9**, 6144–6152 (2024).
61. Kumar, R. & Amanchukwu, C. Active learning accelerates electrolyte solvent screening for anode-free lithium metal batteries. Zenodo. <https://doi.org/10.5281/zenodo.16174975> (2025).

Acknowledgements

This work was supported by the National Science Foundation (NSF) CAREER Award (CBET-2144454). C.V.A. acknowledges the Neubauer Family Assistant Professor program for supporting open access costs. This work made use of the shared facilities (Raman and SEM) at the University of Chicago Materials Research Science and Engineering Center, supported by the National Science Foundation under award number DMR-2011854. NMR measurements were performed at the UChicago Chemistry NMR Facility. XPS was performed at Northwestern University's Atomic and Nanoscale Characterization Experimental Center (NUANCE). The authors thank the Research Computing Center (RCC) at the University of Chicago and Argonne Leadership Computing Facility (ALCF) at Argonne National Laboratory for providing the required computational facilities. The authors thank Steve Trask and Andrew Jansen at Argonne's Cell Analysis, Modeling, and Prototyping (CAMP) facility for providing electrodes. R. K. acknowledges support from the Eric and Wendy Schmidt AI in Science Postdoctoral Fellowship, a Schmidt Sciences program.

Author contributions

C.V.A., P.M., and R.K. conceived the project. P.M. and R.K. contributed equally to the work. P.M. prepared coin cells and conducted battery testing for in-house electrolytes, and all electrolytes from batches 2 to 7, synthesized molecules, and performed NMR and SEM characterizations. R.K. curated and featurized datasets, implemented code for the BMA technique and the overall AL framework, trained GPs, and performed SHAP analysis. K.-H. W. prepared coin cells and conducted battery testing for batch 1 electrolytes and performed XPS characterization. All authors contributed to data analysis, discussion of results, and writing of the manuscript.

Competing interests

The authors declare no competing interests.

Additional information

Supplementary information The online version contains supplementary material available at <https://doi.org/10.1038/s41467-025-63303-7>.

Correspondence and requests for materials should be addressed to Chibueze V. Amanchukwu.

Peer review information *Nature Communications* thanks Shoichi Matsuda, Yangang Liang and the other, anonymous, reviewer(s) for their contribution to the peer review of this work. A peer review file is available.

Reprints and permissions information is available at <http://www.nature.com/reprints>

Publisher's note Springer Nature remains neutral with regard to jurisdictional claims in published maps and institutional affiliations.

Open Access This article is licensed under a Creative Commons Attribution-NonCommercial-NoDerivatives 4.0 International License, which permits any non-commercial use, sharing, distribution and reproduction in any medium or format, as long as you give appropriate credit to the original author(s) and the source, provide a link to the Creative Commons licence, and indicate if you modified the licensed material. You do not have permission under this licence to share adapted material derived from this article or parts of it. The images or other third party material in this article are included in the article's Creative Commons licence, unless indicated otherwise in a credit line to the material. If material is not included in the article's Creative Commons licence and your intended use is not permitted by statutory regulation or exceeds the permitted use, you will need to obtain permission directly from the copyright holder. To view a copy of this licence, visit <http://creativecommons.org/licenses/by-nc-nd/4.0/>.

© The Author(s) 2025